Proceedings of International Mechanical Engineering Congress & Exposition
IMECE 2020
November 15 - 19, 2020, Portland, Oregan, USA

IMECE2020-24237

A LINEAR ACOUSTIC PHASED ARRAY FOR NONRECIPROCAL TRANSMISSION AND RECEPTION

R. Adlakha[1], M. Moghaddaszadeh[2], M. A. Attarzadeh[1], A. Aref[2], M. Nouh[1]*
[1]Department of Mechanical and Aerospace Engineering
[2]Department of Civil, Structural and Environmental Engineering
University at Buffalo (SUNY), Buffalo, NY 14260-4400

ABSTRACT

Acoustic phased arrays are capable of steering and focusing a beam of sound via selective coordination of the spatial distribution of phase angles between multiple sound emitters. Here, we propose a controllable acoustic phased array with space-time modulation that breaks time-reversal symmetry, and enables phononic transition in both momentum and energy spaces. By leveraging the dynamic phase modulation, the proposed linear phased array is no longer bound by the reciprocity principle, and supports asymmetric transmission and reception patterns that can be tuned independently. Through theoretical and numerical investigations, we develop and verify a mathematical framework to characterize the nonreciprocal phenomena, and analyze the frequency conversion between the wave fields. The space-time acoustic phased array facilitates unprecedented control over sound waves in a variety of applications including underwater telecommunication.

1. INTRODUCTION

Reciprocity is a fundamental principle in linear time-invariant systems which dictates identical transmitted and received fields for forward and backward wave propagation [1, 2]. On the other hand, instigating a nonreciprocal behavior opens up exciting possibilities which can positively impact applications in various physical fields ranging from electromagnetics [3–5], to elastic structures [6–8] and acoustics [9–11]. In the latter, methods to break reciprocity include nonlinearities (i.e., exploiting higher order harmonics [12–14]), linear momentum bias by moving the medium [15–17], as well as space-time modulations [18–22]. A linear phased array typically consists of multiple sources distributed along a line and is able to steer an acoustic beam in a prescribed direction [23, 24]. Owing to their capabilities, such phased arrays have been explored in applications including LIDAR [25], RADAR [26], SONAR [27], as well as ultrasound imaging [28, 29]. In general, phased arrays are capable of operating in both transmission and reception modes. However, owing to time-reversal symmetry, traditional phased arrays exhibit identical transmission and reception patterns which limits the scope of their operation. In the optics field, there exists a number of studies which demonstrate a nonreciprocal wave behavior in phased array antennas and meta-surfaces [30–33]. These efforts, however and to the best of our knowledge, have not carried over to the acoustics domain. In this paper, we introduce an acoustic phased array for nonreciprocal acoustic transmission and reception. Such an array makes use of simultaneous space and time periodic variation of phase gradient to break time-reversal symmetry and provide independent control on reception and transmission operation modes.

The paper is organized as follows: Section 2 presents the theory of the space-time periodic (STP) phased array, followed by a full wave analysis of the phased array behavior in both time and frequency domains, which are discussed in Section 3. In Section 4, the theoretical derivations and full wave analysis are validated using a Finite Element solver. Finally, Section 5 provides concluding remarks.

*Corresponding author: mnouh@buffalo.edu

2. THEORY OF SPACE-TIME PHASED ARRAY

The phased array in Fig. 1 comprises N electroacoustic transducers stacked vertically with a center to center distance d. Each transducer is coupled with a phase shifting mechanism which augments the incident signal with a space-time periodic phase angle, $\phi_n(t)$, described by

$$\phi_n(t) = \kappa_s y_n + \Delta\phi \cos(\omega_m t + \kappa_m y_n) \tag{1}$$

where $n = 1, 2, ..., N$ is the transducer index, κ_s is the static phase shift coefficient, y_n is the vertical position of the n^{th} transducer along the array, $\Delta\phi$ is the modulation depth, ω_m is the temporal modulation frequency, and κ_m is the spatial modulation frequency. In transmission mode, the phased array generates acoustic pressure waves into the free space from the input voltage signal as depicted by the green arrows in Fig. 1. The array can also operate in the reception (listening) mode as indicated by the red arrows. The dual-mode operation aligns with the real world applications of phased arrays where, for instance, underwater telecommunication in submarines relies on both transmitted and reflected signals to navigate and identify obstacles. As such, the ability to perform both tasks independently is of great importance. In the following subsections, we lay out the theoretical frame-work describing the breakage of reciprocal symmetry, hence achieving different and independently controllable transmission and reception patterns.

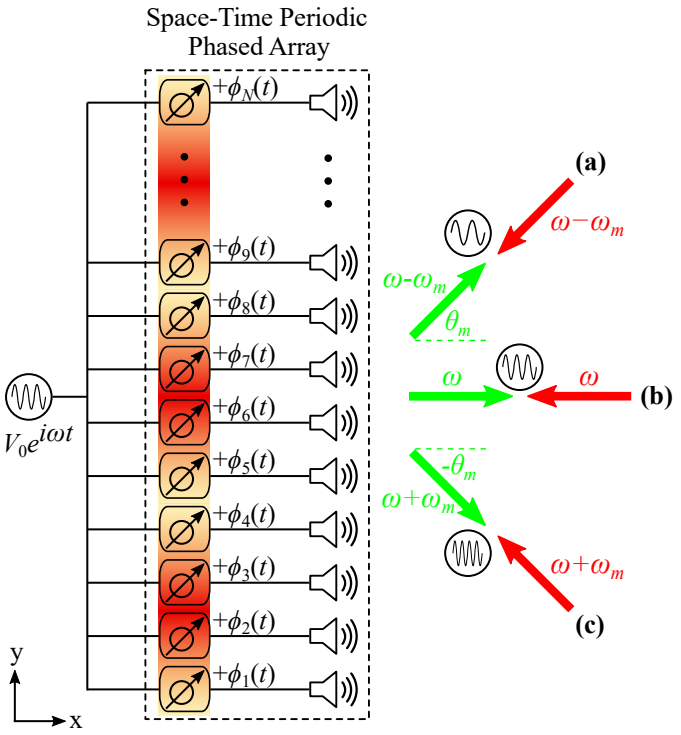

FIGURE 1: Space-time periodic phased array in both transmission and reception modes. (a-c) Lower side, carrier, and upper side bands, respectively. Color gradient in the phase-shifters represents the space-time periodic modulation.

2.1 Transmission Mode

Assuming a time harmonic excitation, the input voltage supplied to the transducers is $V_o e^{i\omega t}$, where $i = \sqrt{-1}$ is the imaginary unit, V_o is the amplitude of the supplied voltage, and ω is the excitation angular frequency. The STP phase-shifters impart an additional time periodic phase angle described by Eq. (1) to the input voltage signal prior to feeding it to the transducers. Consequently, the voltage received by the n^{th} transducer is given by

$$V_n(t) = V_o e^{i[\omega t + \phi_n(t)]} \tag{2}$$

Substituting Eq. (1) into Eq. (2) results in

$$V_n(t) = V_o e^{i(\omega t + \kappa_s y_n)} e^{i\Delta\phi \cos(\omega_m t + \kappa_m y_n)} \tag{3}$$

which can be further expanded by using the Jacobi-Anger expansion into an infinite series of Bessel functions

$$V_n(t) = V_o e^{i(\omega t + \kappa_s y_n)} \sum_{p=-\infty}^{+\infty} i^p J_p(\Delta\phi) e^{ip(\omega_m t + \kappa_m y_n)} \tag{4}$$

where $J_p(\bullet)$ denotes the p^{th}-order Bessel function of the first kind. For small values of $\Delta\phi$, the contributions from higher order terms is negligible compared to the zeroth and first order components, thus yielding

$$V_n(t) = J_o(\Delta\phi) V_o e^{i(\omega t + \kappa_s y_n)} + i\, J_1(\Delta\phi) V_o \left[e^{i(\omega+\omega_m)t + (\kappa_s+\kappa_m)y_n} + e^{i(\omega-\omega_m)t + (\kappa_s-\kappa_m)y_n} \right] \tag{5}$$

In Eq. (5), we only retained the zeroth order (i.e. $J_0(\bullet)$) as well as the first-order (i.e. $J_{\pm1}(\bullet)$) Bessel functions, by using the identity, $J_{-p} = (-1)^p J_{+p}$, and discarded higher order contribu-

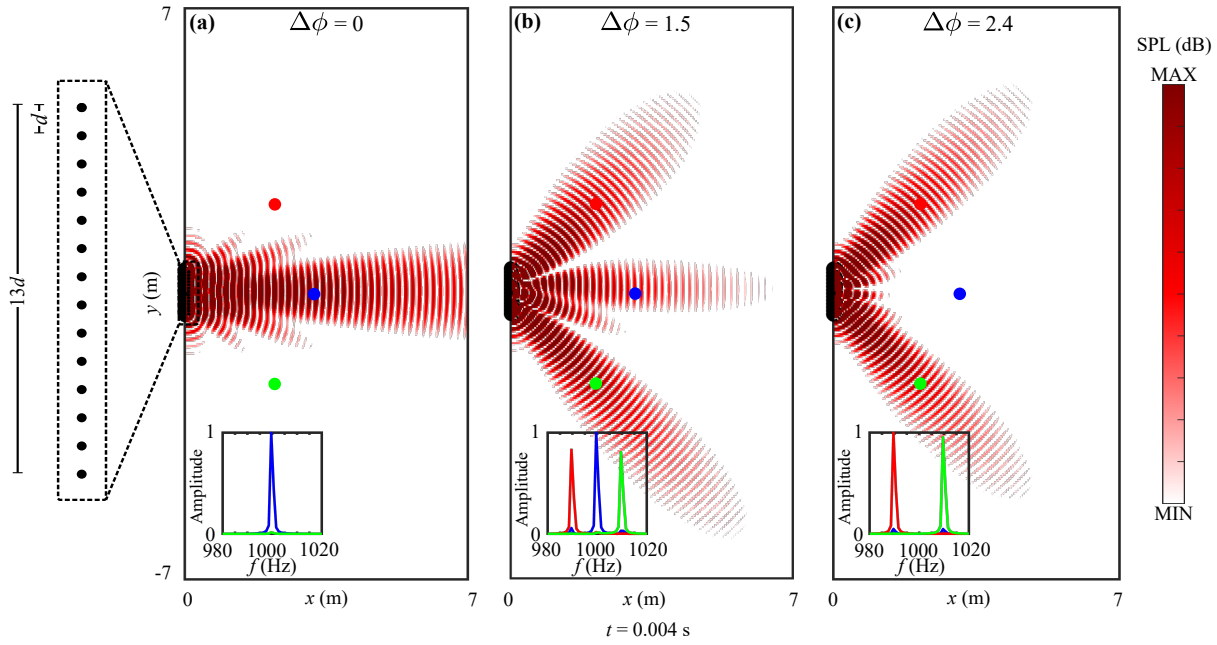

FIGURE 2: The time transient acoustic field sound pressure level (SPL) is illustrated at time $t = 0.004$ s for $\Delta\phi =$ (a) 0, (b) 1.5, and (c) 2.4. The input voltage is a narrow band signal with carrier frequency $f = 1000$ Hz and a static phase shift $\kappa_s = 0$. The temporal and spatial modulation frequencies are $f_m = 10$ Hz and $\kappa_m = 3.92\pi$ rad/m, respectively. κ_m is designed to generate sidebands traveling at $\pm 45^\circ$ from the broadside. The normalized frequency spectrum of the pressure wave at sensor locations marked in red (45°), blue (0°) and green (-45°) are shown in the spectral analysis plots.

tions. The validity of this assumption depends on the values of $\Delta\phi$ and ω_m, i.e., the depth and speed of the phase modulation, respectively. We examine this assumption by using finite element simulations in the sections that follow. Assuming transducers remain in the linear range of operation and exhibit a relatively flat frequency response, the voltage generated by each phase-shifter (given by Eq. (5)) is expected to create an equivalent acoustic pressure wave (i.e, same frequency content and phase gradient). Hence, it can be shown that the pressure field created by the n^{th} transducer at a distance r_n away from the transducer is approximately given by

$$p_n(\mathbf{r}_n, t) = \frac{p_o}{|\mathbf{r}_n|} e^{-i\boldsymbol{\kappa}.\mathbf{r}_n} \Big\{ J_o(\Delta\phi)\, e^{i(\omega t + \kappa_s y_n)} + i\, J_1(\Delta\phi) \big[e^{i(\omega+\omega_m)t + (\kappa_s+\kappa_m)y_n} + e^{i(\omega-\omega_m)t + (\kappa_s-\kappa_m)y_n} \big] \Big\} \tag{6}$$

where p_o is the maximum amplitude of the pressure wave generated by the transducer at an input voltage amplitude of V_o, and $\boldsymbol{\kappa}$ is the wave vector and $\mathbf{r}_n$ is the position vector. From Eq. (6), it is evident that due to the STP phase modulation, the proposed phased array creates side bands in addition to the carrier band with the fundamental frequency ω. It is noted, however, that the static phase shift is carried over to all of the wave components. The side bands have an effective frequency $\omega \pm \omega_m$ and a phase gradient of $(\kappa_s \pm \kappa_m)d$, which results in waves propagating in $\theta_s \mp \theta_m$. The $\pm$ denotes an up-shift and down-shift conversion, respectively.

By assuming that $\mathbf{r}$ is sufficiently greater than the dimensions of the array, the net acoustic pressure field around the phased array can be obtained by simply adding the pressure generated by the individual transducers, which results in

$$p_{\text{net}}(\mathbf{r}, t) = \sum_{n=1}^{N} p_n(\mathbf{r}, t) \tag{7}$$

This expression is effectively used in Sec. 3 to predict behavior of the phased array at arbitrary points in space.

2.2 Reception Mode

In reception mode, the acoustic wave field arriving at the transducers is converted back into multiple electrical signals and is sent through the STP phase-shifters to be collected at the out-

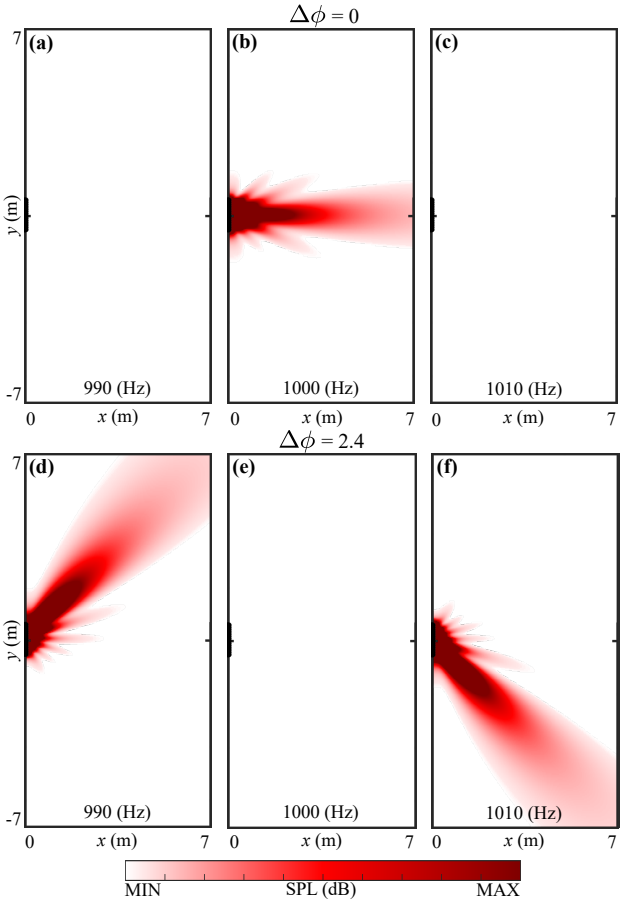

FIGURE 3: Spatial distribution of temporal FFT amplitudes at 990, 1000, and 1010 Hz when phase-shifters are modulated with $\Delta\phi = 0$ (top row) and 2.4 (bottom row). (a-c) $J_0 = 1$ and $J_1 = 0$, transducers generate acoustic waves with carrier frequency only. (d-f) $J_0 = 0$ and $J_1 = 0.52$, transducers generate acoustic waves with higher and lower side bands only, which undergo a directional phase shift after passing through the phased array.

put. To study the behaviour of the array while operating in this mode, we consider the first upper side band (Fig. 1c) and its corresponding phase gradient which is incident on the transducers at an angle θ_m. After passing through the transducers and the STP phase shifters, the output voltage for the n^{th} transducer is described by

$$\hat{V}_n(t) = \hat{V}_\text{o} e^{i[(\omega+\omega_m)t-(\kappa_s+\kappa_m)y_n+\phi_n(t)]} \tag{8}$$

where $\hat{V}_\text{o}$ is the generated voltage amplitude. By substituting $\phi_n(t)$ from Eq. (1) and expanding Eq. (8) by the Jacobi-Anger series, and neglecting contributions from higher order Bessel components, we get

$$\begin{aligned}\hat{V}_n(t) =& J_\text{o}(\Delta\phi)\,\hat{V}_\text{o}\, e^{i[(\omega+\omega_m)t-\kappa_m y_n]} \\ &+i\,J_1(\Delta\phi)\hat{V}_\text{o}\big[e^{i(\omega+2\omega_m)t} + e^{i(\omega t-2\kappa_m y_n)}\big]\end{aligned} \tag{9}$$

Similar equations can be derived for the first lower side band and carrier band in reception mode.

2.3 Acoustic nonreciprocity

A comparison between the output voltage given by Eq. (9) and the originally supplied voltage in radiation mode ($V_\text{o}e^{i\omega t}$) reveals that three types of nonreciprocal behavior can be envisioned: (1) *Momentum nonreciprocity*: The third term in Eq. (9) has the same temporal component ($e^{i\omega t}$) as the original input voltage but is augmented with a phase angle that is equal to $-2\kappa_m y_n$. (2) *Frequency nonreciprocity*: The second term in Eq. (9) ($e^{i(\omega+2\omega_m)t}$) propagates backward along the same direction as the original input (broadside), albeit with a doubly up-converted temporal frequency equal to $\omega + 2\omega_m$. Such a conversion is of great interest in signal processing and filter design, among others. Finally, (3) *Double nonreciprocity*: Both frequency content and the phase angle of the output voltage from each transducer in the first term of Eq. (9), i.e., $e^{i[(\omega+\omega_m)t-\kappa_m y_n]}$, is modified in comparison to the original signal source by the amounts ω_m and $-\kappa_m y_n$, respectively. The latter is effectively a combination of the first and the second nonreciprocities. A similar nonreciprocal behavior can be expected from the phased array when subject to other backward propagating wave components from different directions. For instance, analogous to Eq. (9), the output voltage signal when the lower side band (Fig. 1a) propagates backward, its respective frequency and momentum display all of the three aforementioned categories. This reads

$$\begin{aligned}\hat{V}_n(t) = J_\text{o}(\Delta\phi)\hat{V}_\text{o}e^{i[(\omega-\omega_m)t+\kappa_m y_n]} + iJ_1(\Delta\phi)... \\ \hat{V}_\text{o}[\, e^{i(\omega t+2\kappa_m y_n)} + e^{i(\omega-2\omega_m)t}]\end{aligned} \tag{10}$$

As anticipated, if the carrier band with fundamental frequency is subject to broadside incidence, the resulting voltage components are different than the original signal as given by

$$\begin{aligned}\hat{V}_n(t) = J_\text{o}(\Delta\phi)\hat{V}_\text{o}e^{i\omega t} + iJ_1(\Delta\phi)... \\ \hat{V}_\text{o}[\, e^{i[(\omega+\omega_m)t+\kappa_m y_n]} + e^{i[(\omega-\omega_m)t-\kappa_m y_n]}]\end{aligned} \tag{11}$$

which signifies the independent control over the transmission and reception modes.

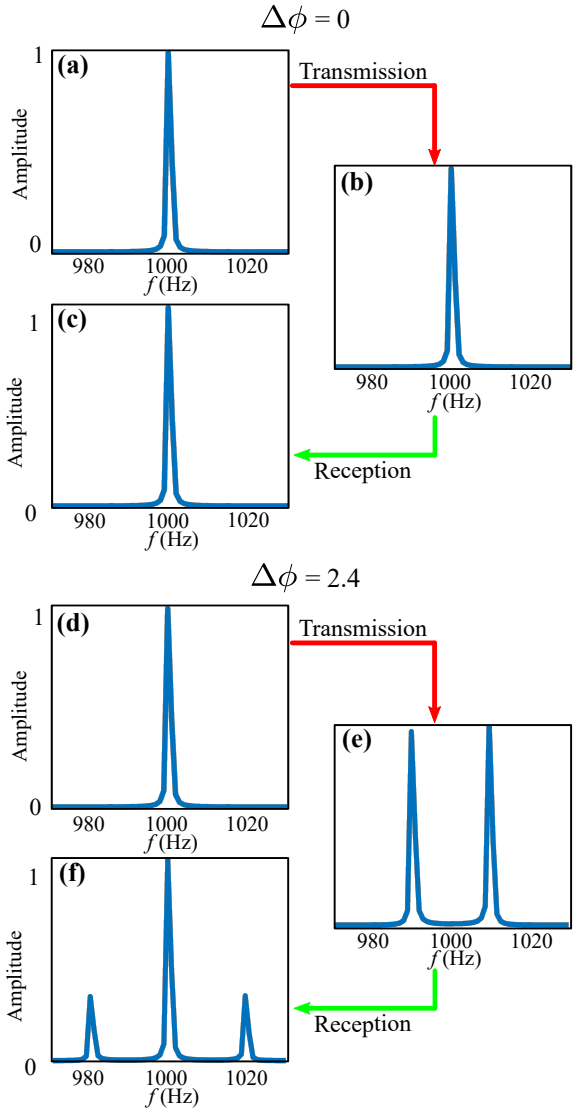

FIGURE 4: FFT of the transducers' voltage signals for transmission and reception corresponding to (a-c) $\Delta\phi = 0$ and (d-f) 2.4. (a) and (d) show the FFT of input signal in transmission, which contains the carrier frequency only. (b) and (e) display the FFT of transmitted acoustic field for both $\Delta\phi = 0$ and 2.4 obtained from the output of the transmission mode. Assuming the same field is incident on the phased array, (c) and (f) show the frequency spectrum of the output voltage signal read from the phased array transducers in the reception mode.

3. FULL WAVE SIMULATIONS AND DISCUSSIONS

In this section, the developed mathematical framework is implemented in an in-house MATLAB code to simulate the array response. We consider an STP phased array of 14 equidistant monopole sources spaced a quarter wavelength apart with a center-to-center distance $d = 85$ mm. The voltage source supplies a narrow band excitation at $f = \omega/2\pi = 1000$ Hz, and the static phase shift κ_s is set equal to zero to simplify the presentation. The monopoles are coupled with STP phase-shifters described by Eq. (1) and are illustrated in Fig. 1. The phase-shifters are temporally modulated at $f_m = 10$ Hz. Every six transducers form one spatial unit cell of the phased array, which leads to a spatial modulation frequency of $\kappa_m = 3.92\pi$ rad/m. As a result, the traveling velocity of the modulation wave is defined as $v = \frac{\omega_m}{\kappa_m} = 5.1$ m/s, which is about two orders of magnitude less than the speed of sound in air. To numerically simulate the acoustic pressure field in the transmission mode, we use the net acoustic pressure expression given by Eq. (7) to compute the far-field acoustic pressure. At first, a set of full-wave time-transient simulations are carried out for three different modulation depths, namely $\Delta\phi = 0,\ 1.5$ and 2.4.

As explained earlier, the values of the Bessel functions $J_{0,1,...}$ determine the contributions from each wave component and the resultant frequency content. This implies that in transmission, the intensities of the carrier and side band depend on the values of $J_0(\Delta\phi)$ and $J_1(\Delta\phi)$, respectively. As such, the Bessel functions of the first kind evaluated at the aforementioned $\Delta\phi$ values are: $J_0(0) = 1$, $J_1(0) = 0$, $J_0(1.5) = 0.51$, $J_1(1.5) = 0.56$, $J_0(2.4) = 0$, and $J_1(2.4) = 0.52$. Fig. 2 shows the simulated transient Sound Pressure Level (SPL) for different values of $\Delta\phi$ at $t = 0.004s$. Fig. 2a shows the carrier band propagating predominantly along the broadside. As soon as $\Delta\phi$ is increased to 1.5, the upper and lower side bands appear in the propagation pattern depicted in Fig. 2b. It is noted that these two wave components propagate at different angles than the carrier band, namely $-45°$ and $+45°$ angles. For $\Delta\phi = 2.4$, however, only the upper and lower side bands propagate while the main carrier band is becomes suppressed, as illustrated in Fig. 2c. The close-up insets in Figs. 2a, b and c show the normalized Fast Fourier Transform (FFT) amplitude of the pressure waves at three distinct sensor locations marked by the blue, green, and red circles. The sensors are positioned along the same radius at $0°$, $-45°$ and $45°$ from the broadside. Given the near-complete suppression of the main carrier wave at $\Delta\phi = 2.4$, we limit the analysis of the STP phased arrays to this modulation depth for the rest of the paper, with the goal of demonstrating how they can be best utilized to achieve efficient control over transmission and reception patterns. Fig. 3 shows the spatial distribution of the FFT amplitude for the carrier band, upper side band and lower side band corresponding to $\Delta\phi = 2.4$. The performance of a traditional phased array ($\Delta\phi = 0$) is shown in the top panel of the same figure for reference. As can be seen, while the traditional phased array allows the main carrier to travel freely, the STP phased array up-converts and down-coverts the carrier band and guides it along $\mp 45°$ channels. Assuming successive frequency transitions from transmission to the reception, Fig. 4 shows FFT

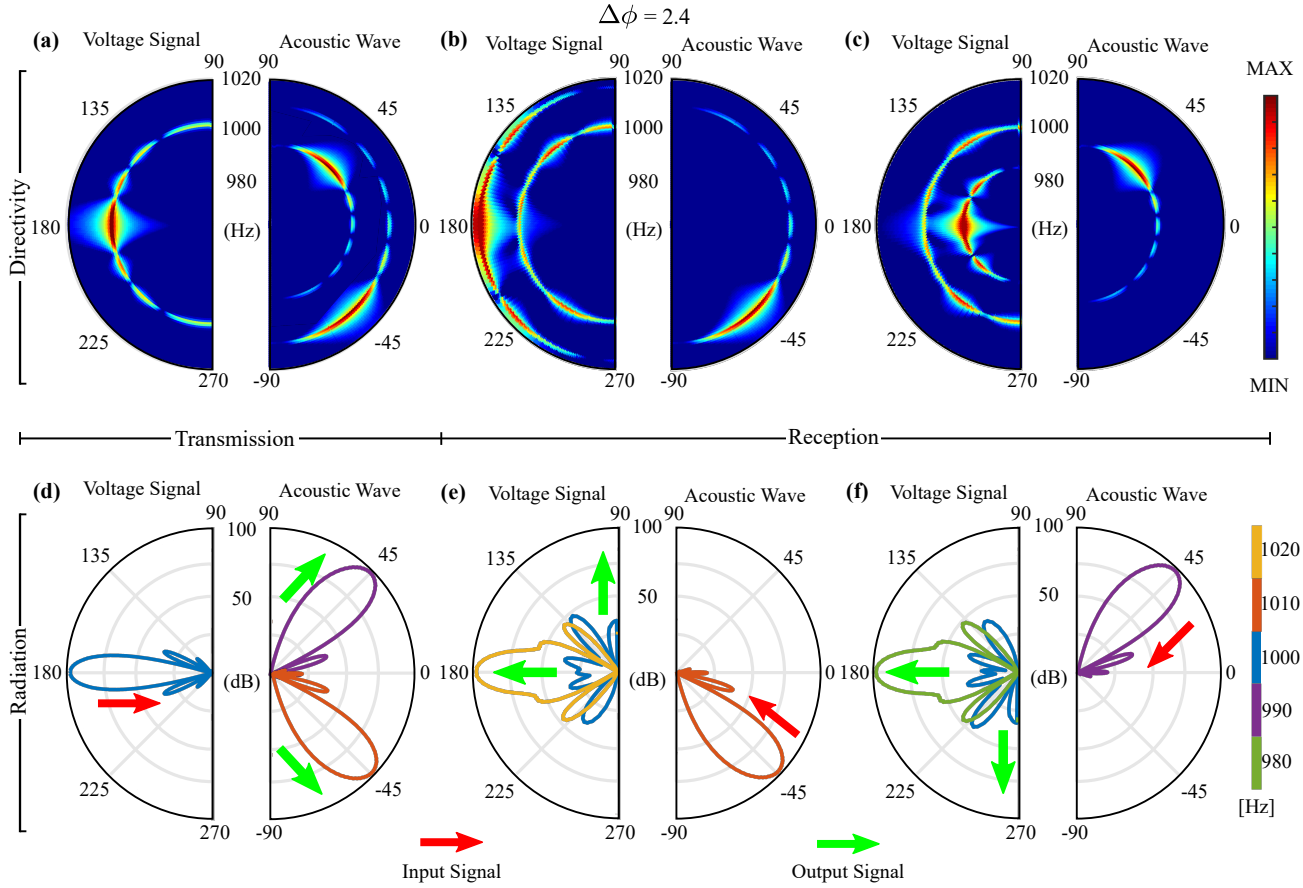

FIGURE 5: Directivity and Radiation patterns in both transmission and reception for an STP phased array with $\Delta\phi = 2.4$. (a) and (d) Array operating in transmission mode. A carrier wave with frequency $f = 1000$ Hz is fed to the array (red arrow) and the resultant field comprises a lower and a upper sideband, traveling at $\pm 45°$ directions from the broadside (green arrows). (b) and (e) Array operating in reception mode. A wave with $f = 1010$ Hz is incident on the array (red arrow) from $-45°$ and the resultant field comprises two wave components traveling along the $\pm 0°$ and $90°$ directions. (c) and (f) Array operating in reception mode. A wave with $f = 990$ Hz is incident on the array from $-45°$ (red arrow) and the resultant field comprises two wave components traveling along $0°$ and $270°$ directions.

results for $\Delta\phi = 2.4$ compared to the traditional phased array. In transmission and then reception, the frequency content of the input voltage signal with frequency $f = 1000$ Hz is conserved when $\Delta\phi = 0$. On the other hand for a $\Delta\phi = 2.4$, successive transmission and reception results into fractions of energy being converted to upper and lower side bands. In this case, side bands with 1010 and 990 Hz appear in the received signal compared to the original source wave, which is in full agreement with the theoretical predictions outlined earlier.

Fig. 5 shows the directivity and radiation patterns for $\Delta\phi = 2.4$ within both transmission and reception operation regimes. The radial axis on the directivity plots denotes the frequency with the intensity represented by the shown color bar. The signal received by all transducers is illustrated in a similar fashion for ease of visualization. Figs. 5d-f show the patterns of transmission and reception for $\Delta\phi = 2.4$. The normalized acoustic pressure field is depicted in the radial direction. The frequency contents for the different wave components are color coded. When a $f = 1000$ Hz voltage signal is supplied to the STP phased array, the directivity and radiation patterns are illustrated in Fig. 5a. The imparted voltage signal results into generation of acoustic pressure waves with the upper and lower side bands traveling at $-45°$ and $+45°$ directions. The direction of the arrows in Fig. 5d indicates the traveling direction of the signal. Figs. 5b and e capture the operation of the STP phased array in the reception mode. In the latter case, the upper side band (red arrow on Fig. 5e) is incident on the phased array in a direction which is the exact reverse of the transmission. The wave carries a 1010 Hz frequency con-

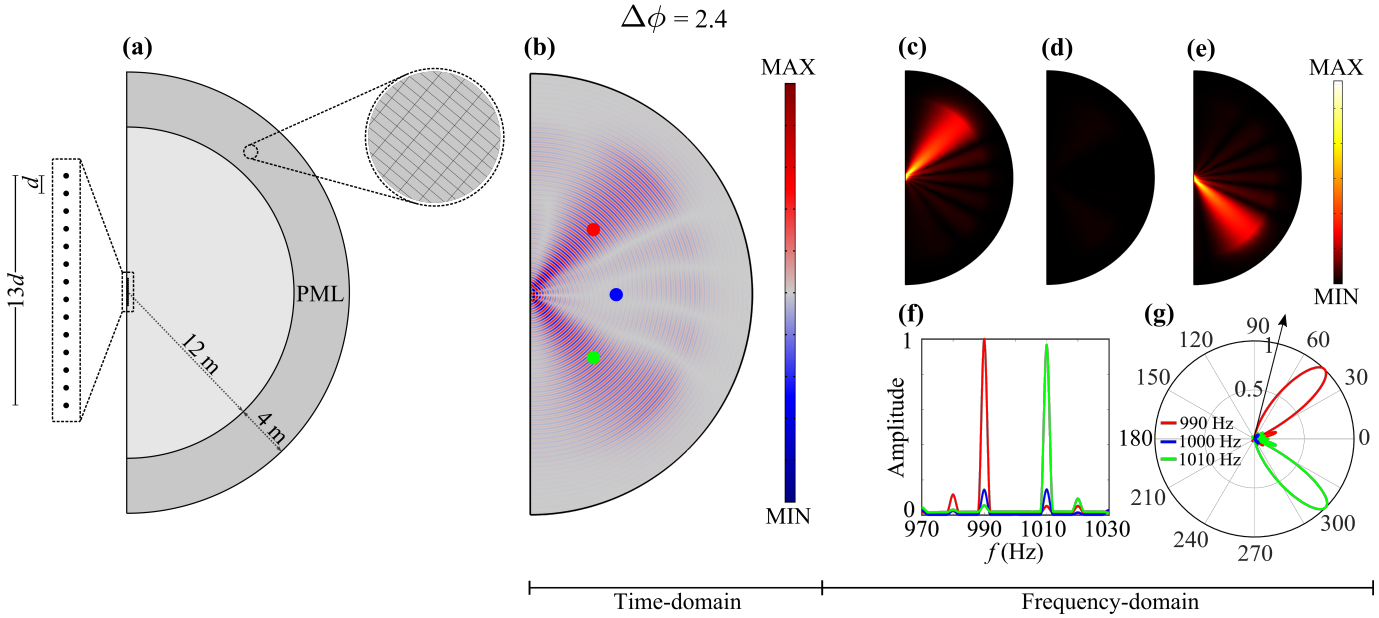

FIGURE 6: Time domain finite element simulations of the STP phased array for a modulation depth of $\Delta\phi = 2.4$: (a) Details related to the considered acoustic domain, monopole sources and close-up of the PML mesh. (b) Pressure field of the STP phased array at $t = 0.05$ s. (c-e) Spatial distribution of FFT amplitudes at $f = 990$ Hz, 1000 Hz and 1010 Hz, respectively. (f) Normalized frequency spectrum of the pressure amplitude for the sensor locations indicated in (b). (e) Normalized FFT amplitude radiation pattern calculated at different frequencies.

tent and a phase angle of $-45°$. Upon passage through the array, the output voltage comprises dominant spectra at $f = 1000$ and 1020 Hz. It can be seen from the radiation plot in Fig. 5e, that $f = 1020$ Hz has an up-converted phase angle resulting in a dominant voltage signal with zero phase angle, which is a manifestation of the *frequency nonreciprocity*. Meanwhile the phase angle of $f = 1000$ Hz is down-converted giving rise to a voltage phase of $-90°$ or, *momentum nonreciprocity*. Similarly, Figs. 5c and f demonstrate the directivity and radiation patterns when a lower side band is back-propagating towards the array with an incident angle of 45° resulting in similar frequency and momentum nonreciprocal effects.

4. NUMERICAL VALIDATION

In order to confirm the theoretical derivation and full-wave simulations provided in previous sections, a number of finite element numerical simulations are performed using COMSOL Multiphysics. The results for the STP phased array with $\Delta\phi = 2.4$ are presented in Fig. 6. A two-dimensional domain composed of a half circle of radius 12 m is considered. The domain is filled with air at a sonic speed of $c = 343$ m/s and a density $\rho = 1.2$ kg/m^3. It is surrounded by a Perfectly Matched Layer (PML) of thickness 4 m, as demonstrated in Fig. 6a, to prevent back-scattering of acoustic waves and mimic free-space conditions. The rest of the simulation parameters are consistent with those stated in Sec. 3. After carrying a mesh sensitivity analysis, a mesh size of roughly $\frac{1}{5}$ of the wavelength is selected with quadratic Lagrange elements to completely capture inter-harmonic couplings and higher-order harmonic generations. It is noted that all finite element simulations are carried out with the space-time modulated phase angle given in Eq. (1) and no approximations are made. This in particular is important since it will enable a reasonable evaluation of the assumptions made in the theoretical section which resulted in Eq. (5). The real-time pressure field of the STP acoustic phased array is depicted in Fig. 6b, showing two different propagation paths at $+45°$ and $-45°$ as predicted by Eq. (6) and earlier shown in Fig. 2. In Figs. 6c-e, a series of FFTs are carried out on the time-domain results and the spatial distribution of FFT amplitudes are shown for the lower side band ($f = 990$ Hz), carrier band ($f = 1000$ Hz), and the upper side band ($f = 1010$ Hz). Furthermore, the normalized FFT spectrum of selected points marked on Fig. 6a are depicted in Fig. 6f. As predicted by the expansion in Eq. (6), different wave components are propagate in different directions. Finally, the radiation patterns of different bands are computed at the exterior field—located on the interior boundary of the PML layer— and are plotted in Fig. 6g. A near-perfect agreement can be observed with the set of results provided earlier.

5. CONCLUSIONS

In this work, a linear acoustic phased array was proposed which provides independent control of transmission and reception patterns, opening up the possibility of nonreciprocal operation. Unlike its conventional counterpart, the space-time periodic phased array is capable of generating additional side bands that carry higher and lower harmonics. The phased array comprises multiple paired up phase-shifters and transducers that are stacked to form a subwavelength device. The phase-shifters are dynamically modulated to follow a space-time periodic pattern with a modulation that travels relatively slower than the speed of sound. The operational principle of the phased array was developed through theoretical derivation and Jacobi-Anger series expansion. Additionally, we demonstrated the dual operation of the space-time periodic phased array in both transmission and reception modes. Through multiple numerical simulations, various possible ways of breaking wave reciprocity have been illustrated and the control over the directivity of transmitted and received waves was shown. The proposed phased array can be of great value to practical applications involving acoustic telecommunication, underwater navigation as well as sea bed research.

Acknowledgement

The authors acknowledges support of this research from the US National Science Foundation through awards no. 1847254 (CAREER) and 1904254.

REFERENCES

[1] Lorentz, H. A., 1896. "The theorem of poynting concerning the energy in the electromagnetic field and two general propositions concerning the propagation of light". *Amsterdammer Akademie der Wetenschappen,* ***4***, p. 176.

[2] Achenbach, J., and Achenbach, J., 2003. *Reciprocity in elastodynamics*. Cambridge University Press.

[3] Adam, J. D., Davis, L. E., Dionne, G. F., Schloemann, E. F., and Stitzer, S. N., 2002. "Ferrite devices and materials". *IEEE Transactions on Microwave Theory and Techniques,* ***50***(3), pp. 721–737.

[4] Sounas, D. L., and Alù, A., 2017. "Non-reciprocal photonics based on time modulation". *Nature Photonics,* ***11***(12), pp. 774–783.

[5] Shupe, D. M., 1980. "Thermally induced nonreciprocity in the fiber-optic interferometer". *Applied optics,* ***19***(5), pp. 654–655.

[6] Attarzadeh, M., Callanan, J., and Nouh, M., 2020. "Experimental observation of nonreciprocal waves in a resonant metamaterial beam". *Phys. Rev. Applied,* ***13***, Feb, p. 021001.

[7] Attarzadeh, M. A., and Nouh, M., 2018. "Elastic wave propagation in moving phononic crystals and correlations with stationary spatiotemporally modulated systems". *AIP Advances,* ***8***(10), p. 105302.

[8] Attarzadeh, M., AlBabaa, H., and Nouh, M., 2018. "On the wave dispersion and non-reciprocal power flow in space-time traveling acoustic metamaterials". *Applied Acoustics,* ***133***, pp. 210 – 214.

[9] Li, X.-F., Ni, X., Feng, L., Lu, M.-H., He, C., and Chen, Y.-F., 2011. "Tunable unidirectional sound propagation through a sonic-crystal-based acoustic diode". *Physical review letters,* ***106***(8), p. 084301.

[10] Boechler, N., Theocharis, G., and Daraio, C., 2011. "Bifurcation-based acoustic switching and rectification". *Nature materials,* ***10***(9), pp. 665–668.

[11] Yang, Z., Gao, F., Shi, X., Lin, X., Gao, Z., Chong, Y., and Zhang, B., 2015. "Topological acoustics". *Physical review letters,* ***114***(11), p. 114301.

[12] Popa, B.-I., and Cummer, S. A., 2014. "Non-reciprocal and highly nonlinear active acoustic metamaterials". *Nature communications,* ***5***(1), pp. 1–5.

[13] Liang, B., Guo, X., Tu, J., Zhang, D., and Cheng, J., 2010. "An acoustic rectifier". *Nature materials,* ***9***(12), pp. 989–992.

[14] Liang, B., Yuan, B., and Cheng, J.-c., 2009. "Acoustic diode: Rectification of acoustic energy flux in one-dimensional systems". *Physical review letters,* ***103***(10), p. 104301.

[15] Fleury, R., Sounas, D., Haberman, M. R., and Alu, A., 2015. "Nonreciprocal acoustics". *Acoustics Today,* ***11***(ARTICLE), pp. 14–21.

[16] Fleury, R., Sounas, D. L., Sieck, C. F., Haberman, M. R., and Alù, A., 2014. "Sound isolation and giant linear nonreciprocity in a compact acoustic circulator". *Science,* ***343***(6170), pp. 516–519.

[17] Godin, O. A., 1997. "Reciprocity and energy theorems for waves in a compressible inhomogeneous moving fluid". *Wave motion,* ***25***(2), pp. 143–167.

[18] Shen, C., Li, J., Jia, Z., Xie, Y., and Cummer, S. A., 2019. "Nonreciprocal acoustic transmission in cascaded resonators via spatiotemporal modulation". *Physical Review B,* ***99***(13), p. 134306.

[19] Zhu, X., Li, J., Shen, C., Peng, X., Song, A., Li, L., and Cummer, S. A., 2020. "Non-reciprocal acoustic transmission via space-time modulated membranes". *Applied Physics Letters,* ***116***(3), p. 034101.

[20] Fleury, R., Sounas, D. L., and Alù, A., 2015. "Subwavelength ultrasonic circulator based on spatiotemporal modulation". *Physical Review B,* ***91***(17), p. 174306.

[21] Li, J., Shen, C., Zhu, X., Xie, Y., and Cummer, S. A., 2019. "Nonreciprocal sound propagation in space-time modulated media". *Physical Review B,* ***99***(14), p. 144311.

[22] Attarzadeh, M., and Nouh, M., 2018. "Non-reciprocal

elastic wave propagation in 2d phononic membranes with spatiotemporally varying material properties". *Journal of Sound and Vibration,* ***422***, pp. 264–277.

[23] Von Ramm, O. T., and Smith, S. W., 1983. "Beam steering with linear arrays". *IEEE Transactions on Biomedical Engineering,* ***BME-30***(8), pp. 438–452.

[24] Wooh, S.-C., and Shi, Y., 1999. "Optimum beam steering of linear phased arrays". *Wave Motion,* ***29***(3), pp. 245 – 265.

[25] Poulton, C. V., Yaacobi, A., Cole, D. B., Byrd, M. J., Raval, M., Vermeulen, D., and Watts, M. R., ts , doi = 10.1364/OL.42.004091. "Coherent solid-state lidar with silicon photonic optical phased arrays". *Opt. Lett.,* ***42***(20), Oct, pp. 4091–4094.

[26] Hassanien, A., and Vorobyov, S. A., 2010. "Phased-mimo radar: A tradeoff between phased-array and mimo radars". *IEEE Transactions on Signal Processing,* ***58***(6), pp. 3137–3151.

[27] Yokoyama, T., Henmi, M., Hasegawa, A., and Kikuchi, T., 1998. "Effects of mutual interactions on a phased transducer array". *Japanese Journal of Applied Physics,* ***37***(Part 1, No. 5B), may, pp. 3166–3171.

[28] vonRamm, O. T., and Thurstone, F. L., 1976. "Cardiac imaging using a phased array ultrasound system. i. system design.". *Circulation,* ***53***(2), pp. 258–262.

[29] Nissen, S. E., Grines, C. L., Gurley, J. C., Sublett, K., Haynie, D., Diaz, C., Booth, D. C., and DeMaria, A. N., 1990. "Application of a new phased-array ultrasound imaging catheter in the assessment of vascular dimensions. in vivo comparison to cineangiography.". *Circulation,* ***81***(2), pp. 660–666.

[30] Hadad, Y., and Steinberg, B. Z., 2013. "One way optical waveguides for matched non-reciprocal nanoantennas with dynamic beam scanning functionality". *Optics express,* ***21***(101), pp. A77–A83.

[31] Guo, X., Ding, Y., Duan, Y., and Ni, X., 2019. "Nonreciprocal metasurface with space–time phase modulation". *Light: Science & Applications,* ***8***(1), pp. 1–9.

[32] Cardin, A. E., Silva, S. R., Vardeny, S. R., Padilla, W. J., Saxena, A., Taylor, A. J., Kort-Kamp, W. J., Chen, H.-T., Dalvit, D. A., and Azad, A. K., 2020. "Surface-wave-assisted nonreciprocity in spatio-temporally modulated metasurfaces". *Nature communications,* ***11***(1), pp. 1–9.

[33] Zang, J., Alvarez-Melcon, A., and Gomez-Diaz, J., 2019. "Nonreciprocal phased-array antennas". *Physical Review Applied,* ***12***(5), p. 054008.